Asymmetric Sites on the $ZnZrO_x$ Catalyst for Promoting Formate Formation and Transformation in CO_2 Hydrogenation

Feng, Zhendong; Tang, Chizhou; Zhang, Pengfei; Li, Kun; Li, Guanna; Wang, Jijie; Feng, Zhaochi; Li, Can

DOI
10.1021/jacs.3c02248

Publication date
2023

Document Version
Final published version

Published in
Journal of the American Chemical Society

JACS
JOURNAL OF THE AMERICAN CHEMICAL SOCIETY
pubs.acs.org/JACS
Article

Asymmetric Sites on the $ZnZrO_x$ Catalyst for Promoting Formate Formation and Transformation in CO_2 Hydrogenation

Zhendong Feng, Chizhou Tang, Pengfei Zhang, Kun Li, Guanna Li, Jijie Wang, Zhaochi Feng,* and Can Li*

Cite This: J. Am. Chem. Soc. 2023, 145, 12663−12672
Read Online
ACCESS | Metrics & More | Article Recommendations | Supporting Information

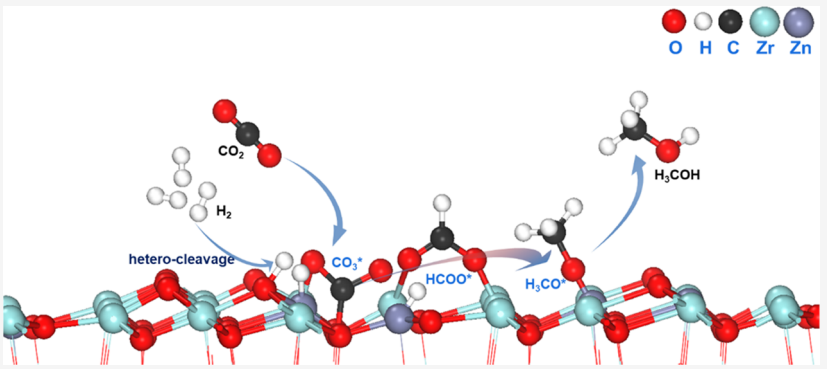

ABSTRACT: The role of formate species for CO_2 hydrogenation is still under debate. Although formate has been frequently observed and commonly proposed as the possible intermediate, there is no definite evidence for the reaction of formate species for methanol production. Here, formate formation and conversion over the $ZnZrO_x$ solid solution catalyst are investigated by in situ/operando diffuse reflectance infrared Fourier transform spectroscopy-mass spectroscopy (DRIFTS-MS) coupled with density functional theory (DFT) calculations. Spectroscopic results show that bidentate carbonate formed from CO_2 adsorption is hydrogenated to formate on Zn−O−Zr sites (asymmetric sites), where the Zn site is responsible for H_2 activation and the Zr site is beneficial for the stabilization of reaction intermediates. The asymmetric Zn−O−Zr sites with adjacent and inequivalent features on the $ZnZrO_x$ catalyst promote not only formate formation but also its transformation. Both theoretical and experimental results demonstrate that the origin of the excellent performance of the $ZnZrO_x$ catalyst for methanol formation is associated with the H_2 heterolytic cleavage promoted by the asymmetric Zn and Zr sites.

1. INTRODUCTION

Catalytic hydrogenation of CO_2 to methanol utilizing green hydrogen produced from renewable energy has attracted intensive attention in view of carbon capture and utilization (CCU).[1−3] An understanding of the reaction mechanism of CO_2 hydrogenation at the molecular level is of great significance to achieve higher CO_2 conversion and methanol selectivity.[4−9] Generally, two reaction pathways,[4,8,10−16] namely, formate (HCOO*) mechanism and CO-involved mechanism, were proposed in the literature where CO was produced from either the RWGS (reverse water gas shift) reaction via HOCO* species or the direct cleavage of the C−O bond in CO_2. It has been proposed that methanol synthesis stems from carboxyl intermediates, while the formate species likely act as a spectator.[9,17,18] However, it was also widely suggested that formate species was the active intermediate for CO_2 hydrogenation.[13,19−21] This conflict about the role of formate usually arises from the easy detection of this species, as it has been observed by extensive measurements.[22,23] For example, some studies have ruled out formate as the active intermediate by comparing the longer residence time of IR features with a mismatched methanol response in MS, but it does not exclude the presence of species subsequent to the reaction of formate, such as the methoxy species. This rarely observed process for formate conversion that has obscured the connection between formate species and methanol formation happens usually under steady-state and ex situ conditions. Thus, it is imperative to obtain the simultaneous responses of surface adsorbates and gaseous products during realistic conditions[5,23−25] (such as formate titration by high-pressure H_2 for its conversion). Another reason leading to the argument is the various adsorbed configurations for formate species. It

Received: March 2, 2023
Published: June 1, 2023

https://doi.org/10.1021/jacs.3c02248
J. Am. Chem. Soc. 2023, 145, 12663−12672

has been reported that bidentate formate is the typical configuration during this reaction, but monodentate formate or Zn formate (formate adsorbed on Zn atoms)[18,22,27,28] is also reported, which is demonstrated to be readily converted for methanol formation. DFT calculations[19,26] have confirmed that formate formation from CO_2 hydrogenation is a highly exothermic process with a small activation barrier. As a result, the further hydrogenation of formate needs to be effectively activated due to its high chemical stability. Kim[29] et al. reported that the asymmetric adsorption of formate on the active sites weakened its internal C−O bond, which can be easily converted to the C−H bond when compared with symmetric adsorption. Such description is also well matched with the Cu−ZnO catalyst where the Cu−ZnO interface covered with asymmetric sites[30,31] play an important role in CO_2 hydrogenation. Thus, it is reasonable to speculate that the surface sites related to the adsorbed formate have a great effect on its activation.

In addition to formate conversion, the origination of formate species is often overlooked for CO_2 hydrogenation, along with the process of CO_2 adsorption and activation. Several studies[16,29,32,33] have described the model for formate formation via direct CO_2 insertion into the metal−hydride bond without a CO_2 adsorption process. They proposed that CO_2 with a bent structure is distorted and interacted with the hydride through the charge-transfer interaction[32,33] from $H^{\delta-}$ (hydride) to $C^{\delta+}$ (CO_2) and the electrostatic interaction between $M^{\delta+}$ (hydride) and $O^{\delta-}$ (CO_2). As a result, formate is formed through the E−R (Eley−Rideal) mechanism by CO_2 insertion.[29] However, the most stable species derived from CO_2 are usually carbonate and bicarbonate species,[34−36] especially for oxide-type catalysts. It has been often ignored because the formed carbonate or bicarbonate is usually considered an inert species for CO_2 hydrogenation.[20,37] Thus, distinguishing the role of carbonate or bicarbonate species during the formate formation is deserved to understand the kinetic mechanism for CO_2 hydrogenation.

In this work, we study the mechanism of CO_2 hydrogenation on the $ZnZrO_x$ solid solution catalyst with operando DRIFTS-MS and DFT calculations from the very initial process, namely, CO_2 adsorption as carbonate species. Then, formate formation from bidentate carbonate, conversion to methoxy, and finally methanol production are followed under reaction conditions. We found that bidentate carbonate as the stable species formed from CO_2 adsorption on Zn−O−Zr sites (asymmetric sites) can be readily hydrogenated to formate species by active hydrogen on the nearby Zn sites. Different from the adjacent and symmetric sites (Zr−O−Zr sites) on ZrO_2, the asymmetric sites on $ZnZrO_x$ promote not only formate formation but also its transformation. Both theoretical and experimental results demonstrate that the excellent performance of the $ZnZrO_x$ catalyst in methanol formation is due to the promotion of H_2 heterolytic cleavage on the asymmetric Zn and Zr sites.

2. RESULTS AND DISCUSSION

2.1. CO_2 Adsorption. Figure 1 shows the IR spectra of adsorbed CO_2 on $ZnZrO_x$, tetragonal ZrO_2 (t-ZrO_2), monoclinic ZrO_2 (m-ZrO_2), ZrO_2 (prepared by precipitation of zirconium nitrate solutions), and ZnO. The presented broad envelope from 1650 to 1200 cm^{-1} is due to the formed carbonate or bicarbonate species.[34,35] Three bands at 1629, 1420, and 1220 cm^{-1} were observed on the detected samples

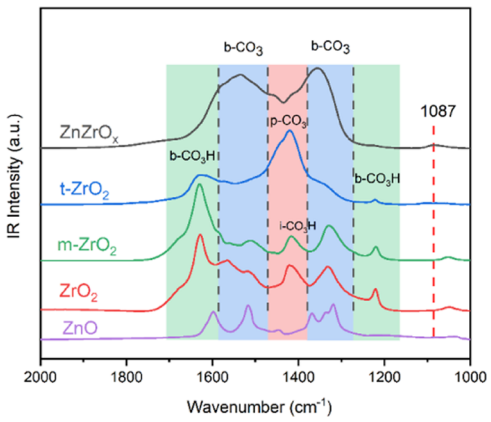

Figure 1. In situ DRIFT spectra taken on different oxides under 0.1 MPa CO_2 at 320 °C. Spectra referenced to different oxides under 0.1 MPa Ar at 320 °C.

except for $ZnZrO_x$ and ZnO. It has been reported that bands at 1629 and 1220 cm^{-1} are assigned to bidentate bicarbonate species (b-CO_3H), whereas 1420 cm^{-1} is assigned to ionic bicarbonate species (i-CO_3H).[34,38] In addition, bands at 1529, 1359, and 1087 cm^{-1} on $ZnZrO_x$, 1095 cm^{-1} on t-ZrO_2, and 1050 cm^{-1} on both m-ZrO_2 and ZrO_2 are assigned to bidentate carbonate species (b-CO_3).[34,35] Comparison of these bands shows the different band shapes and positions of CO_2 adsorption on the $ZnZrO_x$ catalyst, in particular the enhanced b-CO_3. It indicates the different behaviors of CO_2 adsorption on $ZnZrO_x$ with others. It is worth noting that the mono-counterpart ZrO_2 mainly shows the IR bands of b-CO_3H. The different species formed on $ZnZrO_x$ and ZrO_2 indicate the varied properties after introducing ZnO_x into ZrO_2, such as the distribution of surface hydroxyl groups, which is taken into the formation of bicarbonate species.[39] Thus, we tentatively attribute the intensified b-CO_3 on $ZnZrO_x$ to the adsorption of CO_2 on the Zn−O−Zr sites (asymmetric sites).

The shape and band position for the spectra of CO_2 adsorption on ZrO_2 are qualitatively similar to those for m-ZrO_2, suggesting that the ZrO_2 sample prepared by the precipitation method mainly contains the stable monoclinic phase of ZrO_2. Due to the broad extension of IR bands on the $ZnZrO_x$ catalyst, it is difficult to distinguish the definite form of its surface structure. A band position at 1087 cm^{-1} for the $ZnZrO_x$ catalyst that is close to the one of t-ZrO_2 (1095 cm^{-1}) and away from the one of m-ZrO_2 (1050 cm^{-1}) reveals that the topmost atomic structure of $ZnZrO_x$ is reasonably linked to tetragonal ZrO_2, in line with the phase change of ZrO_2 from monoclinic to tetragonal after Zn incorporation (detected by XRD, Figure S1). However, concerning the slight shift of this band between $ZnZrO_x$ and t-ZrO_2 and the great difference in 1650−1200 cm^{-1}, it is proposed that the surface structure of the $ZnZrO_x$ catalyst is likely an amorphous pattern with a distorted tetragonal ZrO_2 and Zn enrichment, which is in agreement with previous reports.[26,40]

CO_2 adsorption on $ZnZrO_x$ with different Zn/Zr atomic ratios indicates similar features to those of m-ZrO_2 when the Zn amount is low (Figure S2). For 13% $ZnZrO_x$, the IR bands of b-CO_3H species disappear. It has been reported that the relative strength of adsorbed b-CO_3H is weaker than that of b-CO_3.[34,35] We thus attributed the variation of b-CO_3H species to the different adsorption strengths of b-CO_3 and b-CO_3H species on $ZnZrO_x$ catalysts. In addition, the adsorbed stability

https://doi.org/10.1021/jacs.3c02248
J. Am. Chem. Soc. 2023, 145, 12663−12672

of b-CO_3 and b-CO_3H was also confirmed by DFT calculations (Tables S1 and S2), which shows that the adsorption energy of b-CO_3 is higher than that of b-CO_3H. On this basis, it is concluded that the principal species formed on the 13% $ZnZrO_x$ catalyst (referred to as $ZnZrO_x$ in the following) is b-CO_3, whereas for the other oxide samples, the principal species are b-CO_3H and b-CO_3.

2.2. Formate Formation. Exposing ZrO_2 to the mixture of CO_2 and H_2 (CO_2/H_2, 1/3) at 320 °C (Figure 2a) shows the

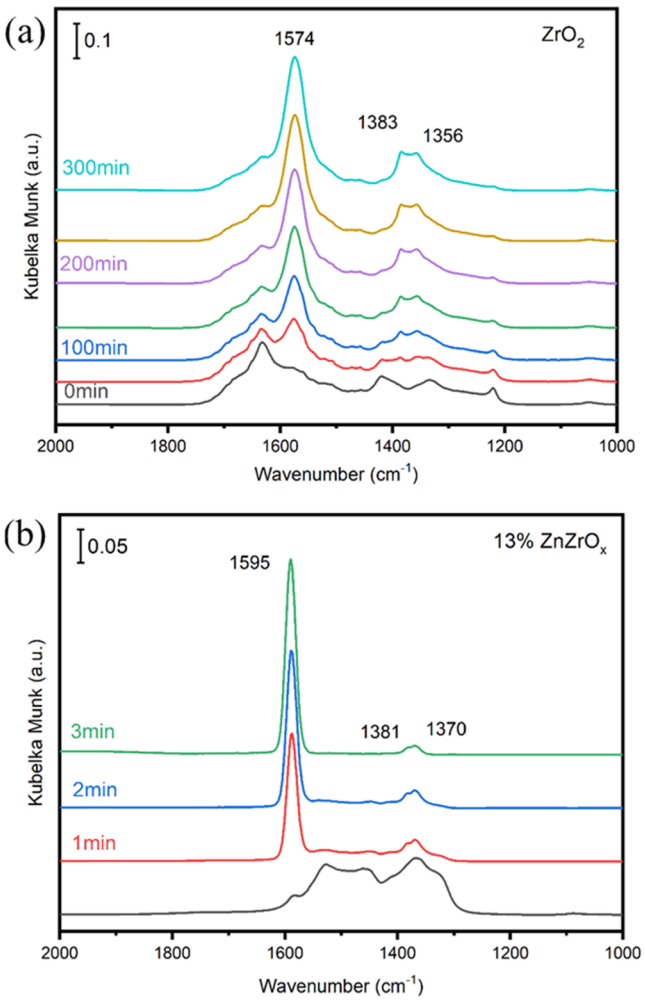

Figure 2. In situ DRIFT spectra taken on (a) ZrO_2 and (b) $ZnZrO_x$ under 1 MPa CO_2/H_2 (1/3) at 320 °C. Spectra referenced to (a) ZrO_2 and (b) $ZnZrO_x$ under 0.1 MPa Ar at 320 °C.

bands of b-CO_3H and b-CO_3 at the initial time, similar to the spectrum of CO_2 adsorption. Four new bands at 1574, 1383 1356, and 2877 cm^{-1} (Figure S3) due to formate species[9,26,34] become discernible after 50 min of reaction. Their intensities increase consistently with time on stream. Correspondingly, the b-CO_3H and b-CO_3 bands gradually attenuate in 300 min. It indicates that carbonate and bicarbonate species are gradually converted to formate on ZrO_2. For $ZnZrO_x$ (Figure 2b), this conversion becomes faster in which carbonate species can be completely converted to formate in 3 min. To reveal the reason for the drastically enhanced rate of formate formation on the Zn-included catalyst, H_2 activation was investigated. H_2−D_2 isotope exchange experiments (Figure 3a) indicate that the initial temperature for HD formation is about to take off at 147 and 250 °C for $ZnZrO_x$ and ZrO_2, respectively, which reveals the lower H_2 activation barrier on the former. Thus, the different formate formation rates for $ZnZrO_x$ and ZrO_2 are attributed to their changed ability of hydrogen activation. In order to obtain molecular insights into H_2 splitting, DFT calculations were also conducted. According to the reported structure,[26] a model for the substitution of one Zr atom by a Zn atom on the most stable t-ZrO_2 (101) surface was constructed for the $ZnZrO_x$ catalyst. For comparison, the results on the m-ZrO_2 (−111) surface (Table S3), which is the main termination exposed by ZrO_2,[45] was used to understand the difference of spectra variations in Figure 2 and H_2−D_2 exchange in Figure 3a. It can be found that the H_2 dissociation on ZrO_2 (Figure 3b) is a highly endothermic process with a dissociative energy of 2.23 eV, while the H_2 dissociation on $ZnZrO_x$ is exothermic with a dissociative energy of −0.07 eV. In addition, the H_2 splitting on $ZnZrO_x$ is further promoted by the lower activation barrier (0.41 eV) than that on ZrO_2 (2.30 eV). This proves that the dissociation of H_2 is thermodynamically and kinetically more favorable on $ZnZrO_x$ than that on ZrO_2. On the other hand, the H_2 splitting on $ZnZrO_x$ is found to be heterolytic, while its cleavage on ZrO_2 is homolytic, in line with the facile formation of the Zn−H bond on ZnO-containing catalysts.[46] The IR spectra of CO_2 hydrogenation on t-ZrO_2 (Figure S4) also show the slow rate of carbonate conversion to formate species, further confirming the importance of Zn species in ZrO_2 patterns. To further confirm the effect of Zn sites on H_2 activation, we performed IR spectra about hydrogen adsorption on ZnO at room temperature. As shown in Figure 3c, the heterolytic cleavage of H_2 with a Zn−H band at 1708 cm^{-1} and an O−H band at 3492 cm^{-1} is observed,[41] confirming the facile dissociation of hydrogen on Zn sites. Calculations about the H_2 activation on ZnO (Figure S5 and Table S4) were also conducted to compare the difference between $ZnZrO_x$ and ZnO. The heterolytic dissociation of H_2 on ZnO was also found to be exothermic (−0.22 eV). But the activation barrier of H_2 activation is slightly higher (0.65 eV) than that on $ZnZrO_x$ (0.41 eV). This proves that the H_2 dissociation on ZnO is kinetically less favorable than that on $ZnZrO_x$. Based on the reported formation of a solid solution catalyst for $ZnZrO_x$,[26] it is proposed that the easier H_2 dissociation is associated with Zn sites that are in the high vicinity of the intrinsic Zr sites on $ZnZrO_x$. High-angle annular dark-field scanning transmission electron microscopy (HAADF-STEM) image and element distribution acquired by energy-dispersive X-ray spectroscopy (EDX) indicate the high dispersion of Zn species on $ZnZrO_x$ (Figure S6). We thus proposed the formation of Zn−O−Zr sites. Combined with the XRD results (Figure S1), which have demonstrated the changed geometric properties of ZrO_2 after adding Zn atoms, we conceived the Zn−O−Zr sites as active sites to have distinct electronic properties for fostering H_2 splitting. On the other hand, the energy difference in the barrier for H_2 activation on $ZnZrO_x$ (0.41 eV) and ZnO (0.65 eV) is negligible compared with the barrier for ZrO_2 (2.30 eV), in good agreement with the similar initial temperature of H_2 dissociation for $ZnZrO_x$ and ZnO and the bigger difference for $ZnZrO_x$ and ZrO_2 (Figure 3a).

We then examined the transformation of carbonate to formate by DFT calculations (Figure 3d). The adsorption energy and activation barriers for formate formation are calculated and compared for $ZnZrO_x$ and ZrO_2. Formate formation on both catalysts is thermodynamically favorable

https://doi.org/10.1021/jacs.3c02248
J. Am. Chem. Soc. 2023, 145, 12663−12672

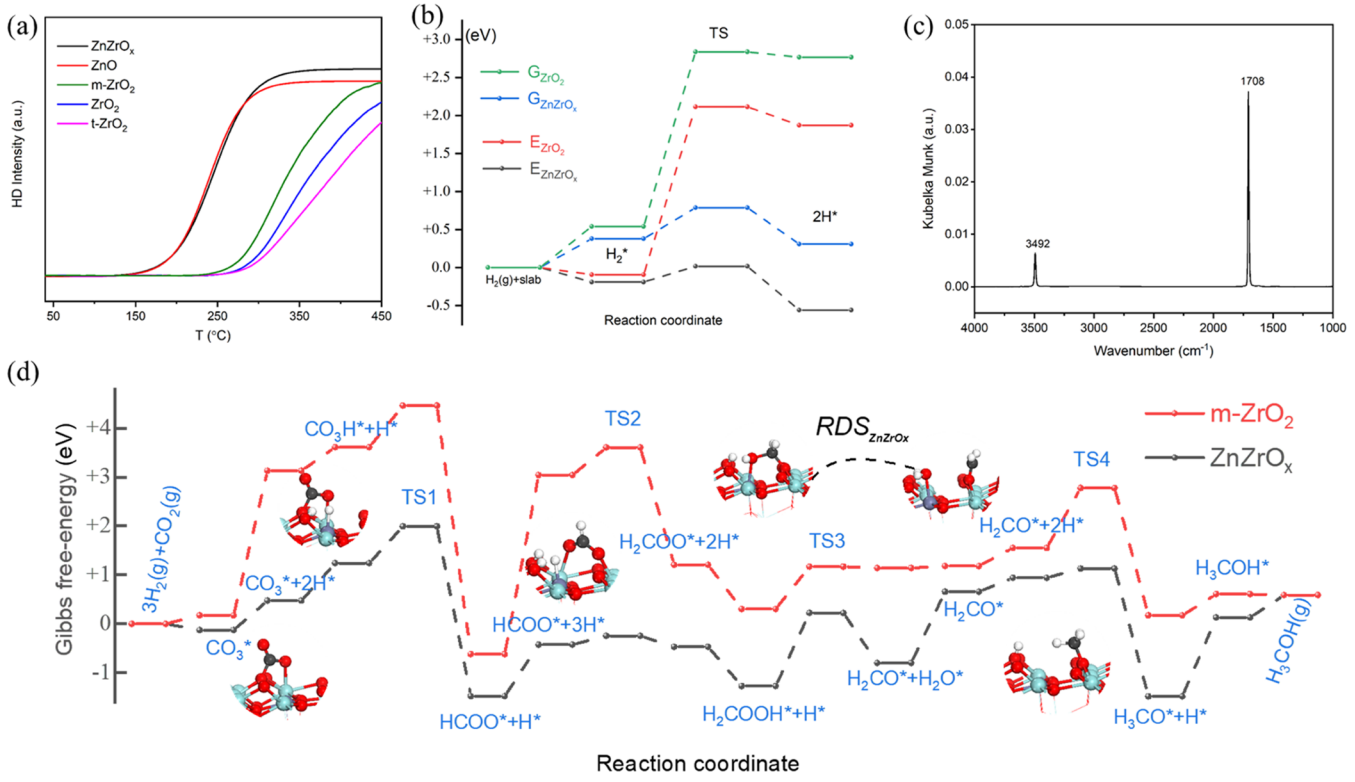

Figure 3. (a) H_2−D_2 isotope exchange reaction on the catalysts. (b) Energy and Gibbs free energy calculated at 593 K for H_2 activation on $ZnZrO_x$ and ZrO_2. Calculated energies are referenced to the surface slab and H_2(g). (c) DRIFT spectra taken on ZnO under H_2 at room temperature. Spectra referenced to ZnO under Ar flow at room temperature. (d) Energy and Gibbs free energy calculated at 593 K for the hydrogenation of CO_2 to methanol on $ZnZrO_x$ and ZrO_2. The calculated energies are referenced to the surface slab and CO_2(g) + 3H_2(g). Atom color: zirconium (cyan), oxygen (red), zinc (gray), carbon (black), and hydrogen (white).

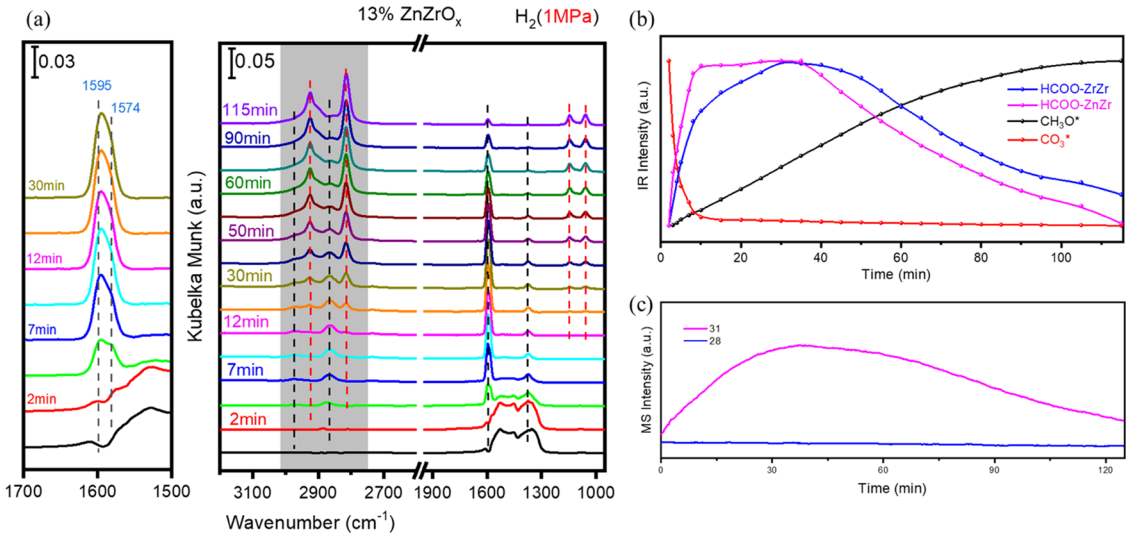

Figure 4. (a) Operando DRIFT spectra and corresponding variation of (b) IR intensity and (c) MS signal taken on $ZnZrO_x$ at 260 °C after switching the feed gas from CO_2 to 1 MPa H_2. Spectra referenced to $ZnZrO_x$ under 0.1 MPa Ar at 260 °C.

with higher formation energies (ΔG calculated between carbonate with hydrogen and formate) of −1.95 and −3.75 eV for $ZnZrO_x$ and ZrO_2, respectively. However, the formate formation is more kinetically favored on $ZnZrO_x$ catalyst due to the lower activation barrier on $ZnZrO_x$ (TS1, 0.75 eV) than ZrO_2 (0.85 eV), consistent with the results in Figure 2. It should be noted that H_2 dissociation also participated in formate formation for both catalysts. It has the highest energy demand and activation barrier (2.30 eV) for ZrO_2. As a result, H_2 activation likely act as the rate-determining step for formate formation on ZrO_2 and not on $ZnZrO_x$. This further demonstrated the indispensable role of Zn−O−Zr sites in H_2 activation. By combining the in situ spectra and the calculated results, it is speculated that on ZrO_2, H_2 activation is constricted, which makes the conversion of carbonate to formate slow, while on the $ZnZrO_x$ catalyst, the faster

https://doi.org/10.1021/jacs.3c02248
J. Am. Chem. Soc. 2023, 145, 12663−12672

formation of active hydrogen promoted by Zn sites leads to the complete hydrogenation of bidentate carbonate to formate species. This means that it is the facile H_2 dissociation related to Zn incorporation that makes the difference in carbonate conversion to formate.

In contrast to the results on ZrO_2, in situ spectra on ZnO during CO_2 hydrogenation mainly show the bands at 2170 and 2110 cm^{-1} for gas-phase CO (Figure S7). Bands for carbonate and formate (1571 cm^{-1}) have also been detected. This indicates that the RWGS reaction is promoted by ZnO particles, in line with high CO selectivity for CO_2 hydrogenation on the ZnO sample (Figure S8). On the other hand, the high dispersion of Zn species on the $ZnZrO_x$ catalyst exhibits higher methanol selectivity than CO, demonstrating that Zn dispersion is beneficial for resisting the RWGS reaction.

2.3. Formate Conversion. In order to gain insights into the evolution of surface species for methanol formation on the $ZnZrO_x$ catalyst, a series of DRIFTS-MS measurements were carried out under transient conditions. Figure 4a shows the spectrum response after switching the feed gas from CO_2 to H_2 under 1 MPa over the $ZnZrO_x$ catalyst. Similar to the results of Figure 2, carbonate was converted to formate upon H_2 introduction. A close inspection of the formate band on $ZnZrO_x$ reveals the superimposition of two bands at 1595 and 1574 cm^{-1} (enlarged picture on the left of Figure 4a). According to the band position of formate in Figure 2 and previous reports,[5,26] the higher band position at 1595 cm^{-1} is assigned to the formate adsorbed on adjacent Zn and Zr sites, while the lower band position at 1574 cm^{-1} is due to the formate adsorbed on neighboring Zr and Zr sites. These assignments are in line with the calculated frequencies (Table S5) for formate adsorbed on different sites. Adsorption energies calculated for formate species (Table S2) indicate that both types of formate formations are exothermic, whereas the latter one binds with the surface with a higher adsorption energy (−0.60 and −1.48 eV). Thus, we assumed that the formate on adjacent Zn and Zr sites would be converted to the stable one on adjacent Zr and Zr sites under reaction conditions, which will expose the Zn sites for splitting hydrogen and put the reaction forward for methanol formation.

In addition to the band at 1595 cm^{-1}, formate bands[26,34] at 1381, 1370, 2977, and 2881 cm^{-1} also increased upon H_2 introduction. About 10 min after the reaction started, bands at 2930 and 2817 cm^{-1} appeared and developed quickly (Figure 4a), which are assigned to asymmetric stretch ν_{as}(C−H) and symmetric stretch ν_s(C−H) in methoxy species, respectively.[26,42,43] Formate intensity reached a plateau at ∼35 min. Meanwhile, two bands at 1145 and 1053 cm^{-1} for methoxy species with terminal and bridged configurations, respectively, were also observed. The increase of methoxy species and the simultaneous decrease of formate species were then observed by MS evolution (Figure 4c). This shows an increase in methanol formation upon switching the gas feed from CO_2 to H_2 (t = 0) with the maximum at ∼35 min, in line with the variation of formate intensity in IR spectra (Figure 4b). D_2 isotope experiments also demonstrate the transformation (Figure S9). These concomitant developments revealed that the formate species was directly responsible for methanol formation. In addition, we can hardly detect the formation of methoxy species nor methanol product on ZrO_2 (Figure S3), and the IR bands for $ZnZrO_x$ under 0.1 MPa H_2 developed tardily and did not reach the steady level even after the reaction for 2 h (Figure S10), which reveals the importance of operando detections.

The reaction profile for methanol formation on $ZnZrO_x$ and ZrO_2 expressed in terms of Gibbs free energy at a typical reaction temperature of 320 °C is also depicted in Figure 3d, and the structures of all adsorbates are presented in Tables S2 and S3. For comparison, the reaction profile in terms of potential energy at 0 K is plotted in Figure S11. For the sake of clarity, the H_2 activation shown in Figure 3b is lumped in a single step in this figure. Following the formate pathway, each point in the free energy diagram for $ZnZrO_x$ lies lower than that for ZrO_2, confirming the more thermodynamically favorable pathway on $ZnZrO_x$. The lowest points in the diagram are formate and methoxy, in good agreement with the experimental data. Combined with the results of operando detection, the formate hydrogenation to methoxy, which is divided into four steps in the following DFT calculation, is proposed to be the rate-determining step (RDS) for methanol formation on $ZnZrO_x$. From the formate adsorbed on the Zn−O−Zr sites, the transfer of active hydrogen from the Zn site can generate H_2COO* species with a low free energy barrier (0.18 eV). Following proton transfer generates H_2COOH* species where its further transformation is the most energetically demanding step with an energy barrier of 1.49 eV. Comparing the results for ZrO_2 on which the rate-determining step is H_2 activation with an activation energy of 2.30 eV, the relative energy barrier for $ZnZrO_x$ is lower. This indicates that the promoted H_2 activation on $ZnZrO_x$ facilitates the intermediate conversion and methanol formation. The analysis of the charge density difference for H_2 dissociation (Figure S12) further confirms the heterolytic cleavage of H_2 with the formation of $Zn-H^{\delta-}$, in good agreement with Figure 3c. It is worth noting that each of the three C−H bonds for methanol formation on $ZnZrO_x$ is kinetically more favorable than ZrO_2. On this basis, the nucleophilic attack of H^- to the C atom in the intermediates, such as CO_3*, HCOO*, and H_2CO*, is proposed to promote the formation of the C−H bond for methanol formation. Therefore, the close bonded Zn−O−Zr sites, on which the Zn site is responsible for H_2 activation and Zr sites are responsible for stabilizing the intermediates, are proposed to promote not only formate formation but also its further transformation. The asymmetric environment of the $ZnZrO_x$ catalyst with adjacent and inequivalent features on the surface is reasonably responsible for methanol formation.

To further confirm the importance of formate species, we have attempted to hydrogenate formate species derived from adsorbed formic acid on the $ZnZrO_x$ catalyst (Figure S13) and compared it with the spectra for CO_2 hydrogenation. Formate bands at 1595 and 2877 cm^{-1} appeared upon the exposure of the catalyst to formic acid. The slight difference in the relative intensity of the hydroxyl group at 3675 cm^{-1} is due to the introduction of water contained in formic acid. The shape and band position of spectra for formic acid hydrogenation under high-pressure H_2 (Figure S14) are qualitatively similar to those for CO_2 hydrogenation (Figure 4), both of which reveal the transformation of formate to methoxy species. In addition, we also compared the spectra of methanol adsorption and CO_2 hydrogenation in a similar way. Methoxy bands at 2925 and 2824 cm^{-1} appeared immediately after the exposure to methanol steam (Figure S13). This indicates that the methoxy species can be definitely regarded as the representative species of methanol. However, the formate band (1595 cm^{-1})

https://doi.org/10.1021/jacs.3c02248
J. Am. Chem. Soc. 2023, 145, 12663−12672

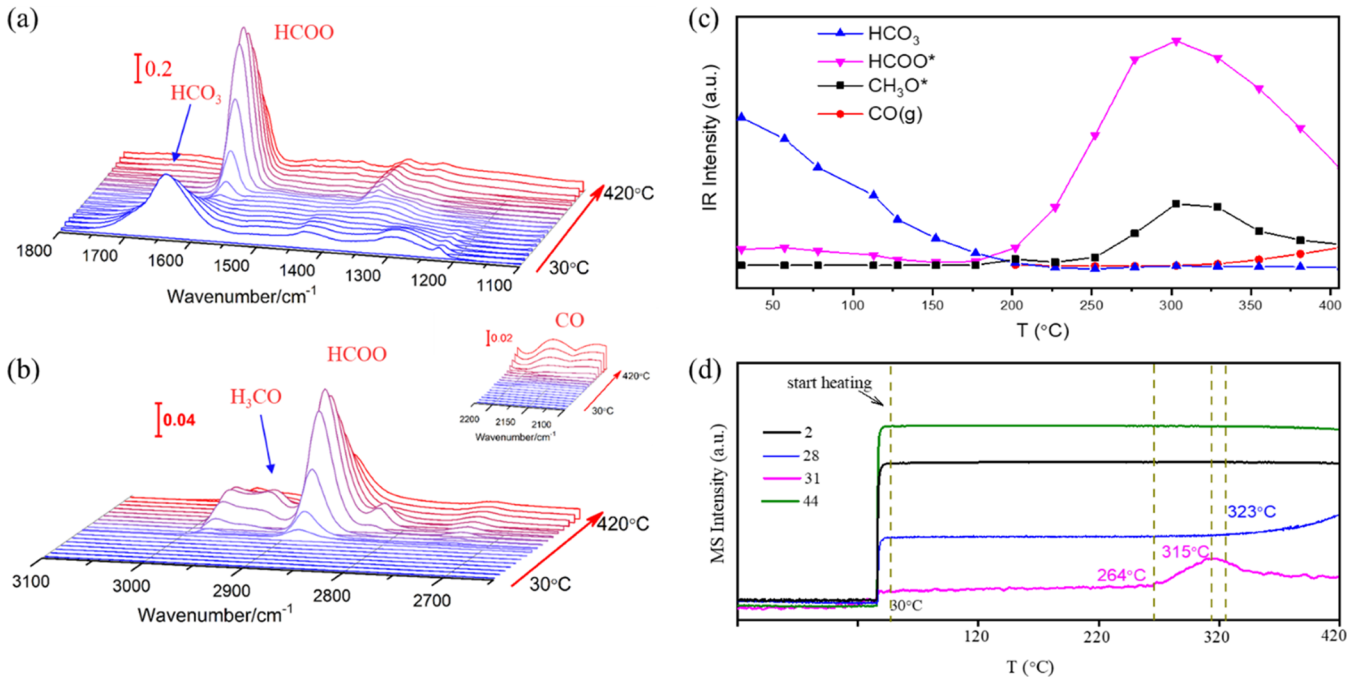

Figure 5. Operando DRIFT spectra in the regions of (a) 1800−1100 cm^{-1} and (b) 3100−2650 cm^{-1} (inset for 2225−2100 cm^{-1}) and corresponding variation of (c) IR intensity and (d) MS signal taken on $ZnZrO_x$ with elevating temperature from 30 to 420 °C under 0.1 MPa CO_2/H_2. Spectra referenced to $ZnZrO_x$ under 0.1 MPa Ar at different temperatures.

appeared later and grew significantly after introducing methanol. It turns out that the reverse conversion of methoxy species to formate takes place easily and the forward hydrogenation of formate to methoxy is possibly the RDS for methanol formation.

In comparison with the transient response, the reaction under a steady flow of mixed gas (CO_2/H_2, 1/3) is much closer to the working conditions. Figure 5 shows the operando results of the temperature-programmed reaction (TPR) for CO_2 hydrogenation on $ZnZrO_x$. It reveals a maximum of formate intensity (1595 cm^{-1}) at 310 °C with the appearance of methoxy species (2930 cm^{-1}) at 250 °C, which increases to its maximum at 320 °C. Variations of MS signals during this course (Figure 5d) display neither CO nor methanol formation before 264 °C. This indicates the higher onset temperature for formate transformation under normal pressure. However, the corresponding temperatures for CO and methoxy formation are, respectively, ∼90 and ∼50 °C lower under 1 MPa conditions (Figure S15), which reveals that high pressure is beneficial for formate conversion, in line with the results of Figures 4 and S8. In addition, a further increase of CO formation is observed at ∼331 °C (Figure S15). It is suggested that the slower CO formation at low temperatures originates from the RWGS reaction, while the rapid increase stems from both the RWGS reaction and formate dissociation. From the detailed illustration of the effects of temperature shown in Figure 6a, we find that a rapid decrease of formate intensity is observed at higher temperatures. Both the normalized intensity of methoxy species and the simultaneous rates for methanol formation exhibit "volcano-type" curves during operando DRIFTS-MS at five selected temperatures between 280 and 360 °C (Figure 6b), which clearly show the qualitative and quantitative results for the formate hydrogenation to methoxy species, corresponding to methanol formation.

Apart from these observations, it is worth mentioning that a weak band appeared at 3016 cm^{-1} for gas-phase CH_4 (Figure S16) under high-pressure H_2. For the realistic reaction, if CO_2 is extracted out of the cell, IR bands of gas-phase CO (Figure S17) disappear, while the band for gas-phase CH_4 (3016 cm^{-1}) remains and even intensifies. Such a different variation indicates the disparate reaction pathways for these two products. Given the retention of gas-phase CH_4, which is accompanied by the conversion of formate to methoxy species, it is proposed that CH_4 and methanol may share the same intermediate and the hydrogenation need to be delicately modified in order to expand the methanol production.

3. CONCLUSIONS

Surface species formed on the $ZnZrO_x$ catalyst for CO_2 hydrogenation to methanol were studied by operando DRIFTS-MS and DFT calculations. The principal species formed from CO_2 adsorption on the $ZnZrO_x$ catalyst is bidentate carbonate on asymmetric (Zn−O−Zr) sites. Spectroscopic results show that Zn−O−Zr sites promote not only formate formation from carbonate hydrogenation with the help of active hydrogen on the nearby Zn sites but also formate transformation to methoxy species, which is responsible for methanol production. From the theoretical and experimental results, the H_2 heterolytic dissociation promoted by the asymmetric sites is proposed to be key for improving the performance of methanol formation on the $ZnZrO_x$ catalyst.

4. EXPERIMENTAL SECTION

4.1. Catalyst Preparation. The $ZnZrO_x$ catalyst was prepared by the co-precipitation method. For a 13% $ZnZrO_x$ catalyst, a Zn precursor (0.9 g $Zn(NO_3)_2{\cdot}6H_2O$) and a Zr precursor (8.6 g $Zr(NO_3)_4{\cdot}5H_2O$) were dissolved in 200 mL of deionized water under vigorous stirring at 70 °C. Then, 120% excess $(NH_4)_2CO_3$ was added to the solution under stirring at 70 °C with an aqueous solution of 100 mL. The dropping rate was kept dropwise to control the dropping

https://doi.org/10.1021/jacs.3c02248
J. Am. Chem. Soc. 2023, 145, 12663−12672

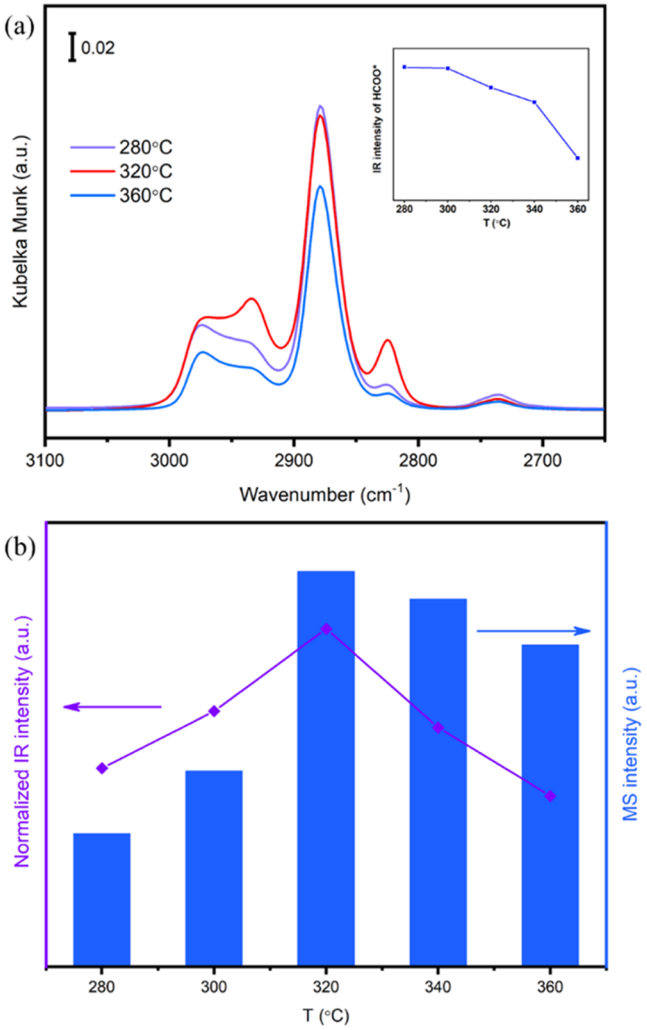

Figure 6. (a) Operando DRIFT spectra taken on $ZnZrO_x$ under 1 MPa CO_2/H_2 (1/3) at different temperatures (inset: IR intensity of formate species as a function of temperature). (b) Normalized IR intensity of adsorbed methoxy and methanol signals of MS as a function of temperature.

rate and finish the dripping within 30 min. After that, the solution was continually stirred to age for 2 h, naturally cooled down, filtered, and repeatedly washed with deionized water. The obtained solid was kept at 110 °C overnight and calcined to 500 °C for 3 h at a heating rate of 5 °C/min. As mentioned above, ZnO sample was synthesized by precipitation of $Zn(NO_3)_2{\cdot}6H_2O$) solution and ZrO_2 sample was synthesized by precipitation of $Zr(NO_3)_4{\cdot}5H_2O$) solution. The preparations of m-ZrO_2 and t-ZrO_2 referred to the reported literature.[44]

4.2. Catalyst Characterization. The XRD results were collected on a Philips PW1050/81 diffractometer operating in Bragg–Brentano focusing geometry and using Cu Ka radiation (l = 1.5418 Å) from a generator operating at 40 kV and 30 mA. High-resolution transmission electron microscopy (HRTEM) and element mappings acquired by energy-dispersive X-ray (EDX) were carried out on a JEM-F200 multipurpose electron microscope at 200 kV. Before measurement, the samples were ultrasonically suspended in ethanol, dripped onto a copper grid-supported transparent carbon foil, and dried in air.

4.3. H_2–D_2 Isotopic Exchange Reaction. The catalyst was reduced by H_2 at 320 °C for 2 h and purged with Ar at 400 °C for 2 h. After that, the temperature was reduced to 30 °C, and the reaction gas was changed to a mixture of H_2 (10 mL/min) and D_2 (10 mL/min) under 0.1 MPa. H_2 (m/z = 2), D_2 (m/z = 4), and HD (m/z = 3) were detected by a mass spectrometer when the temperature was increased to 500 °C with a heating rate of 5 °C/min.

4.4. In Situ Diffuse Reflectance Infrared Fourier Transform Spectroscopy (DRIFTS). DRIFTS was conducted on a Fourier transform spectrometer (Bruker VERTEX 80V), equipped with a mercury cadmium telluride (MCT) detector. The measurement was carried out in a high-temperature reaction chamber (Harrick Scientific) equipped with ZnSe windows. Each spectrum was recorded at 4 cm^{-1} resolution with an average of 64 scans, and all spectra were obtained in Kubelka–Munk (KM) units. In a typical measurement, the catalyst was reduced by H_2 at 320 °C for 2 h with a flow rate of 20 mL/min and purged with Ar within 20 mL/min at 400 °C for 2 h. After that, the temperature was reduced to the detected temperature under an Ar atmosphere to collect the background, followed by exposing the catalyst to different reaction gases to collect spectra. For CO_2 and H_2 adsorption on ZnO, it was calcined in an O_2 atmosphere at 500 °C before cooling to the detected temperature.

4.5. DRIFTS of the Hydrogenation Process at Different H_2 Pressures. To gain insights into the change process of surface species, DRIFTS were conducted at 260 °C. Before each measurement, the sample was reduced by H_2 at 320 °C for 2 h with a flow rate of 20 mL/min and purged with Ar within 20 mL/min at 400 °C for 2 h. Then, the sample was cooled to 260 °C in Ar in order to obtain the background spectrum. DRIFTS were first collected after switching Ar to CO_2 with normal pressure for 30 min. Subsequently, the reactor was purged with Ar for 10 min to remove the residual gas CO_2, and DRIFTS were conducted under H_2 exposure with different pressures.

4.6. DRIFTS with Elevating Temperature. To gain the effect of temperature, DRIFTS were conducted with elevating temperature. Before each measurement, the sample was reduced by H_2 at 320 °C for 2 h with a flow rate of 20 mL/min and purged with Ar within 20 mL/min at 400 °C for 2 h. Then, the sample was cooled to 30 °C in Ar and a series of background spectra were obtained every 10 min under Ar with a temperature-increasing rate of 3 °C/min. After that, the sample was recooled to 30 °C in Ar and exposed to CO_2/H_2. The same collecting time and increasing rate were applied to obtain the IR spectra, which were subtracted by the spectra with the same temperature under Ar to reduce the effect of heat radiation.

4.7. Operando Measurements of DRIFTS and MS (Mass Spectroscopy). MS measurements were carried out in conjunction with DRIFTS detection. In a typical MS detection, the signals of selected m/z were recorded as a function of reaction time.

4.8. Catalyst Evaluation. The activity evaluation of CO_2 hydrogenation to methanol is carried out on a fixed tubular bed with a gas chromatograph connected in series. Before the reaction, 0.1 g of the catalyst and 0.4 g of quartz sand are uniformly mixed and reduced under a H_2 atmosphere at 320 °C for 2 h. The reaction is carried out under $V(H_2)/V(CO_2)/V(Ar)$ = 72/24/4 and GHSV = 32 000 mL/(g h) at different temperatures and pressures. The tail gas of the reaction tube is insulated at 150 °C and connected to the chromatograph (Agilent GC-7890B), equipped with TCD and FID detectors.

4.9. DFT (Density Functional Theory) Calculations. Spin-polarized DFT calculations were performed by using the Vienna Ab initio Simulation Package (VASP) with generalized gradient approximation based on the Perdew–Burke–Ernzerhof (PBE) exchange–correlation density functional.[47] Valence electrons were described with a plane-wave energy cutoff of 500 eV, whereas core electrons were represented by projector augmented wave (PAW) pseudopotentials. Gaussian smearing of the population of partial occupancies with a width of 0.1 eV and the Grimme-D3 dispersion correction were included to treat van der Waals interactions. Geometry optimization was performed by setting the threshold for energy convergence to 10^{-5} eV until the forces on each atom were less than 0.05 eV/Å. The minimum-energy reaction pathways and the corresponding transition states were determined using the nudged elastic band method with an improved tangent estimate (CI-NEB).[48] The frequency analysis of the stationary points was performed by means of the finite difference method as implemented in VASP. Small displacements (0.02 Å) were used to estimate the numerical Hessian

https://doi.org/10.1021/jacs.3c02248
J. Am. Chem. Soc. 2023, 145, 12663–12672

matrix. Frequency analysis was also performed for transition states by confirming the presence of a single imaginary frequency corresponding to the specific reaction path.

The lattice parameter for m-ZrO_2 (a = 5.17 Å, b = 5.25 Å, c = 5.32 Å) and t-ZrO_2 ($a = b$ = 3.63 Å, c = 5.24 Å) were fully optimized in the first step by using a γ-centered (6 × 6 × 6) and (8 × 8 × 6) k-point mesh with a higher cutoff energy. The m-ZrO_2 (−111)[45] and t-ZrO_2 (101)[26] surface slab model was modeled as a periodically repeated p (2 × 3) slab with three O−Zr−O layers, separated by a vacuum layer of 15 Å along the surface normal direction and optimized using a γ-centered (2 × 2 × 1) k-point mesh. For the $ZnZrO_x$ catalyst, a Zr atom on the t-ZrO_2 (101) surface was replaced by a Zn atom. Considering the valence difference of Zn^{2+} and Zr^{4+}, an oxygen vacancy adjacent to Zn^{2+} was also introduced. In each optimization, the outermost O−Zr−O layer was allowed to relax, whereas the two bottommost layers were fixed in their bulk positions. H_2 activation on the ZnO catalyst was also calculated on the nonpolar (10−10) surface, which is the most stable facet reported for ZnO.[49] Before H_2 adsorption, the lattice parameter of ZnO ($a = b$ = 3.29 Å, c = 5.30 Å) was first optimized by using a γ-centered (8 × 8 × 6) k-point mesh with a higher cutoff energy. The surface slab model was modeled as a periodically repeated p (3 × 2) slab with a vacuum layer of 15 Å along the surface normal direction. During the optimization, the topmost ZnO layer was allowed to relax, while the bottom layers were fixed in their bulk positions.

The binding energy of the reaction intermediates was calculated as $\Delta E_{ads} = E_{adsorbate+surface} - E_{adsorbate} - E_{clean-surface}$, and the described adsorption energy is referred to as the energy of initial reactants in the gas phase. The activation energy (ΔE_a) of a chemical reaction was defined as the energy difference between the initial and transition states, whereas the reaction energy (ΔE) was defined as the energy difference between the initial and final states. The Gibbs free energy for a given species is $G(T, P) = E_e + E_{trans} + E_{rot} + E_{vib} + PV\text{-}T$ ($S_{trans} + S_{rot} + S_{vib}$), where

$$E_{trans} = \frac{3}{2}RT$$

$$E_{rot} = RT \times 1(\text{linear molecule})$$

$$E_{rot} = RT \times \frac{2}{3}(\text{nonlinear molecule})$$

$$E_{vib} = R\sum_n \frac{h\upsilon_n}{K_B}\left(\frac{1}{2} + \frac{1}{e^{h\upsilon_n/K_BT} - 1}\right)$$

$$S_{trans} = R\left(\ln\frac{\left(\frac{2\pi mK_BT}{h^2}\right)^{3/2}K_BT}{p} + \frac{5}{2}\right)$$

$$S_{rot} = R\left(\ln\left(\frac{1}{\sigma}\left(\frac{8\pi^2K_BT}{h^2}\right) \times I\right) + 1\right)(\text{linear molecule})$$

$$S_{rot} = R\left(\ln\left(\frac{\sqrt{\pi}}{\sigma}\left(\frac{8\pi^2K_BT}{h^2}\right)^{2/3} \times \sqrt{I_x \times I_y \times I_z}\right) + \frac{2}{3}\right)$$

(nonlinear molecule)

$$S_{vib} = R\sum_n \left(\frac{\frac{h\upsilon_n}{K_BT}}{e^{h\upsilon_n/K_BT} - 1}\right) - \ln(1 - e^{-h\upsilon_n/K_BT})$$

Here, I is the moment of inertia, σ is the rotational symmetry number, and m is the mass of the molecule. The translational, rotational, and vibrational enthalpic and entropic contributions of gas-phase molecules were calculated by considering them as ideal gases. For adsorbed molecules and transition states on the surface, the rotational and translational contributions were converted into vibration modes. The PV term of the surface species was approximated to be negligible because it was very small with regard to other energetic terms, and thus, we considered $G(T, P) = E_e + E_{vib} - T \times S_{vib}$ in the calculations.

■ ASSOCIATED CONTENT

Supporting Information

The Supporting Information is available free of charge at https://pubs.acs.org/doi/10.1021/jacs.3c02248.

DFT results; IR spectra; and catalytic data, including Tables S1−S5 and Figures S1−S17 (PDF)

■ AUTHOR INFORMATION

Corresponding Authors

Zhaochi Feng − *State Key Laboratory of Catalysis, Dalian Institute of Chemical Physics, Chinese Academy of Sciences, Dalian 116023, China*; Email: zcfeng@dicp.ac.cn

Can Li − *State Key Laboratory of Catalysis, Dalian Institute of Chemical Physics, Chinese Academy of Sciences, Dalian 116023, China; University of Chinese Academy of Sciences, Beijing 100049, China*; orcid.org/0000-0002-9301-7850; Email: canli@dicp.ac.cn

Authors

Zhendong Feng − *State Key Laboratory of Catalysis, Dalian Institute of Chemical Physics, Chinese Academy of Sciences, Dalian 116023, China; University of Chinese Academy of Sciences, Beijing 100049, China*

Chizhou Tang − *State Key Laboratory of Catalysis, Dalian Institute of Chemical Physics, Chinese Academy of Sciences, Dalian 116023, China; University of Chinese Academy of Sciences, Beijing 100049, China*

Pengfei Zhang − *State Key Laboratory of Catalysis, Dalian Institute of Chemical Physics, Chinese Academy of Sciences, Dalian 116023, China*

Kun Li − *State Key Laboratory of Catalysis, Dalian Institute of Chemical Physics, Chinese Academy of Sciences, Dalian 116023, China*

Guanna Li − *Catalysis Engineering, Department of Chemical Engineering, Delft University of Technology, 2629 HZ Delft, Netherlands*; orcid.org/0000-0003-3031-8119

Jijie Wang − *State Key Laboratory of Catalysis, Dalian Institute of Chemical Physics, Chinese Academy of Sciences, Dalian 116023, China*

Complete contact information is available at: https://pubs.acs.org/10.1021/jacs.3c02248

Notes

The authors declare no competing financial interest.

■ ACKNOWLEDGMENTS

The work was also conducted by the Fundamental Research Center of Artificial Photosynthesis (FReCAP), financially supported by the National Natural Science Foundation of China (22088102) and the National Natural Science Foundation of China (22272163). The authors are also grateful to Prof. Li Haiyang and Hou Keyong for their advanced mass spectrometer technology.

■ REFERENCES

(1) Goeppert, A.; Czaun, M.; Jones, J. P.; Surya Prakash, G. K.; Olah, G. A. Recycling of carbon dioxide to methanol and derived products - closing the loop. *Chem. Soc. Rev.* **2014**, *43*, 7995−8048.

(2) Sha, F.; Han, Z.; Tang, S.; Wang, J.; Li, C. Hydrogenation of Carbon Dioxide to Methanol over Non-Cu-based Heterogeneous Catalysts. *ChemSusChem* **2020**, *13*, 6160−6181.
(3) Shih, C. F.; Zhang, T.; Li, J. H.; Bai, C. L. Powering the Future with Liquid Sunshine. *Joule* **2018**, *2*, 1925−1949.
(4) Grabow, L. C.; Mavrikakis, M. Mechanism of Methanol Synthesis on Cu through CO2 and CO Hydrogenation. *ACS Catal.* **2011**, *1*, 365−384.
(5) Fisher, I. A.; Bell, A. T. In-SituInfrared Study of Methanol Synthesis from H2/CO2over Cu/SiO2and Cu/ZrO2/SiO2. *J. Catal.* **1997**, *172*, 222−237.
(6) Fisher, I. A.; Bell, A. T. In Situ Infrared Study of Methanol Synthesis from H2/CO over Cu/SiO2and Cu/ZrO2/SiO2. *J. Catal.* **1998**, *178*, 153−173.
(7) Li, X.; Lin, J.; Li, L.; Huang, Y.; Pan, X.; Collins, S. E.; Ren, Y.; Su, Y.; Kang, L.; Liu, X.; Zhou, Y.; Wang, H.; Wang, A.; Qiao, B.; Wang, X.; Zhang, T. Controlling CO2 Hydrogenation Selectivity by Metal-Supported Electron Transfer. *Angew. Chem., Int. Ed.* **2020**, *59*, 19983−19989.
(8) Kattel, S.; Yu, W.; Yang, X.; Yan, B.; Huang, Y.; Wan, W.; Liu, P.; Chen, J. G. CO2 Hydrogenation over Oxide-Supported PtCo Catalysts: The Role of the Oxide Support in Determining the Product Selectivity. *Angew. Chem., Int. Ed.* **2016**, *55*, 7968−7973.
(9) Kattel, S.; Liu, P.; Chen, J. G. Tuning Selectivity of CO2 Hydrogenation Reactions at the Metal/Oxide Interface. *J. Am. Chem. Soc.* **2017**, *139*, 9739−9754.
(10) Wang, J.; Zhang, G.; Zhu, J.; Zhang, X.; Ding, F.; Zhang, A.; Guo, X.; Song, C. CO2 Hydrogenation to Methanol over In2O3-Based Catalysts: From Mechanism to Catalyst Development. *ACS Catal.* **2021**, *11*, 1406−1423.
(11) Frei, M. S.; Capdevila-Cortada, M.; García-Muelas, R.; Mondelli, C.; López, N.; Stewart, J. A.; Curulla Ferré, D.; Pérez-Ramírez, J. Mechanism and microkinetics of methanol synthesis via CO2 hydrogenation on indium oxide. *J. Catal.* **2018**, *361*, 313−321.
(12) Wang, Y. H.; Gao, W. G.; Wang, H.; Zheng, Y. E.; Na, W.; Li, K. Z. Structure-activity relationships of Cu-ZrO2 catalysts for CO2 hydrogenation to methanol: interaction effects and reaction mechanism. *RSC Adv.* **2017**, *7*, 8709−8717.
(13) Larmier, K.; Liao, W. C.; Tada, S.; Lam, E.; Verel, R.; Bansode, A.; Urakawa, A.; Comas-Vives, A.; Coperet, C. CO2-to-Methanol Hydrogenation on Zirconia-Supported Copper Nanoparticles: Reaction Intermediates and the Role of the Metal-Support Interface. *Angew. Chem., Int. Ed.* **2017**, *56*, 2318−2323.
(14) Noh, G.; Lam, E.; Bregante, D. T.; Meyet, J.; Sot, P.; Flaherty, D. W.; Coperet, C. Lewis Acid Strength of Interfacial Metal Sites Drives CH3 OH Selectivity and Formation Rates on Cu-Based CO2 Hydrogenation Catalysts. *Angew. Chem., Int. Ed.* **2021**, *60*, 9650−9659.
(15) Kattel, S.; Yan, B.; Yang, Y.; Chen, J. G.; Liu, P. Optimizing Binding Energies of Key Intermediates for CO2 Hydrogenation to Methanol over Oxide-Supported Copper. *J. Am. Chem. Soc.* **2016**, *138*, 12440−12450.
(16) Yang, Y.; Evans, J.; Rodriguez, J. A.; White, M. G.; Liu, P. Fundamental studies of methanol synthesis from CO2 hydrogenation on Cu(111), Cu clusters, and Cu/ZnO(0001). *Phys. Chem. Chem. Phys.* **2010**, *12*, 9909−9917.
(17) Yang, Y.; Mei, D.; Peden, C. H. F.; Campbell, C. T.; Mims, C. A. Surface-Bound Intermediates in Low-Temperature Methanol Synthesis on Copper: Participants and Spectators. *ACS Catal.* **2015**, *5*, 7328−7337.
(18) Yang, Y.; Mims, C. A.; Disselkamp, R. S.; Kwak, J.-H.; Peden, C. H. F.; Campbell, C. T. Non)formation of Methanol by Direct Hydrogenation of Formate on Copper Catalysts. *J. Phys. Chem. C* **2010**, *114*, 17205−17211.
(19) Ye, J. Y.; Liu, C. J.; Mei, D. H.; Ge, Q. F. Active Oxygen Vacancy Site for Methanol Synthesis from CO2 Hydrogenation on In2O3(110): A DFT Study. *ACS Catal.* **2013**, *3*, 1296−1306.
(20) Zhu, J. D.; Su, Y. Q.; Chai, J. C.; Muravev, V.; Kosinov, N.; Hensen, E. J. M. Mechanism and Nature of Active Sites for Methanol Synthesis from CO/CO2 on Cu/CeO2. *ACS Catal.* **2020**, *10*, 11532−11544.
(21) Hu, J.; Yu, L.; Deng, J.; Wang, Y.; Cheng, K.; Ma, C.; Zhang, Q.; Wen, W.; Yu, S.; Pan, Y.; Yang, J.; Ma, H.; Qi, F.; Wang, Y.; Zheng, Y.; Chen, M.; Huang, R.; Zhang, S.; Zhao, Z.; Mao, J.; Meng, X.; Ji, Q.; Hou, G.; Han, X.; Bao, X.; Wang, Y.; Deng, D. Sulfur vacancy-rich MoS2 as a catalyst for the hydrogenation of CO2 to methanol. *Nat. Catal.* **2021**, *4*, 242−250.
(22) Zabilskiy, M.; Sushkevich, V. L.; Palagin, D.; Newton, M. A.; Krumeich, F.; van Bokhoven, J. A. The unique interplay between copper and zinc during catalytic carbon dioxide hydrogenation to methanol. *Nat. Commun.* **2020**, *11*, No. 2409.
(23) Vogt, C.; Groeneveld, E.; Kamsma, G.; Nachtegaal, M.; Lu, L.; Kiely, C. J.; Berben, P. H.; Meirer, F.; Weckhuysen, B. M. Unravelling structure sensitivity in CO2 hydrogenation over nickel. *Nat. Catal.* **2018**, *1*, 127−134.
(24) Tarasov, A. V.; Seitz, F.; Schlögl, R.; Frei, E. In Situ Quantification of Reaction Adsorbates in Low-Temperature Methanol Synthesis on a High-Performance Cu/ZnO:Al Catalyst. *ACS Catal.* **2019**, *9*, 5537−5544.
(25) Wang, X.; Shi, H.; Kwak, J. H.; Szanyi, J. Mechanism of CO2 Hydrogenation on Pd/Al2O3 Catalysts: Kinetics and Transient DRIFTS-MS Studies. *ACS Catal.* **2015**, *5*, 6337−6349.
(26) Wang, J.; Li, G.; Li, Z.; Tang, C.; Feng, Z.; An, H.; Liu, H.; Liu, T.; Li, C. A highly selective and stable ZnO-ZrO2 solid solution catalyst for CO2 hydrogenation to methanol. *Sci. Adv.* **2017**, *3*, No. e1701290.
(27) Nakamura, J.; Fujitani, T.; Kuld, S.; Helveg, S.; Chorkendorff, I.; Sehested, J. Comment on "Active sites for CO2 hydrogenation to methanol on Cu/ZnO catalysts". *Science* **2017**, *357*, No. eaan8074.
(28) Beck, A.; Zabilskiy, M.; Newton, M. A.; Safonova, O.; Willinger, M. G.; van Bokhoven, J. A. Following the structure of copper-zinc-alumina across the pressure gap in carbon dioxide hydrogenation. *Nat. Catal.* **2021**, *4*, 488−497.
(29) Kim, Y.; Trung, T. S. B.; Yang, S.; Kim, S.; Lee, H. Mechanism of the Surface Hydrogen Induced Conversion of CO2 to Methanol at Cu(111) Step Sites. *ACS Catal.* **2016**, *6*, 1037−1044.
(30) Bailie, J. E.; Rochester, C. H.; Millar, G. J. Spectroscopic evidence for adsorption sites located at Cu/ZnO interfaces. *Catal. Lett.* **1995**, *31*, 333−340.
(31) Kattel, S.; Ramirez, P. J.; Chen, J. G.; Rodriguez, J. A.; Liu, P. Active sites for CO2 hydrogenation to methanol on Cu/ZnO catalysts. *Science* **2017**, *355*, 1296−1299.
(32) Nakano, H.; Nakamura, I.; Fujitani, T.; Nakamura, J. Structure-Dependent Kinetics for Synthesis and Decomposition of Formate Species over Cu(111) and Cu(110) Model Catalysts. *J. Phys. Chem. B* **2001**, *105*, 1355−1365.
(33) Sakaki, S.; Musashi, Y. An ab initio molecular-orbital study of insertion of CO2into a RhI−H bond. *J. Chem. Soc., Dalton Trans.* **1994**, *20*, 3047−3054.
(34) Pokrovski, K.; Jung, K. T.; Bell, A. T. Investigation of CO and CO2 Adsorption on Tetragonal and Monoclinic Zirconia. *Langmuir* **2001**, *17*, 4297−4303.
(35) Bachiller-Baeza, B.; Rodriguez-Ramos, I.; Guerrero-Ruiz, A. Interaction of Carbon Dioxide with the Surface of Zirconia Polymorphs. *Langmuir* **1998**, *14*, 3556−3564.
(36) Schumann, J.; Tarasov, A.; Thomas, N.; Schlogl, R.; Behrens, M. Cu,Zn-based catalysts for methanol synthesis: On the effect of calcination conditions and the part of residual carbonates. *Appl. Catal., A* **2016**, *516*, 117−126.
(37) Nielsen, N. D.; Thrane, J.; Jensen, A. D.; Christensen, J. M. Bifunctional Synergy in CO Hydrogenation to Methanol with Supported Cu. *Catal. Lett.* **2020**, *150*, 1427−1433.
(38) Rhodes, M.; Pokrovski, K.; Bell, A. The effects of zirconia morphology on methanol synthesis from CO and H2 over Cu/ZrO2 catalystsPart II. Transient-response infrared studies. *J. Catal.* **2005**, *233*, 210−220.

https://doi.org/10.1021/jacs.3c02248
J. Am. Chem. Soc. 2023, 145, 12663−12672

(39) Atherton, K.; Newbold, G.; Hockey, J. A. Infra-red spectroscopic studies of zinc oxide surfaces. *Discuss. Faraday Soc.* **1971**, *52*, No. 33.
(40) Wang, J.; Tang, C.; Li, G.; Han, Z.; Li, Z.; Liu, H.; Cheng, F.; Li, C. High-Performance MaZrOx (Ma = Cd, Ga) Solid-Solution Catalysts for CO2 Hydrogenation to Methanol. *ACS Catal.* **2019**, *9*, 10253−10259.
(41) Dong, A.; Lin, L.; Mu, R.; Li, R.; Li, K.; Wang, C.; Cao, Y.; Ling, Y.; Chen, Y.; Yang, F.; Pan, X.; Fu, Q.; Bao, X. Modulating the Formation and Evolution of Surface Hydrogen Species on ZnO through Cr Addition. *ACS Catal.* **2022**, *12*, 6255−6264.
(42) Lee, K.; Anjum, U.; Araújo, T. P.; Mondelli, C.; He, Q.; Furukawa, S.; Pérez-Ramírez, J.; Kozlov, S. M.; Yan, N. Atomic Pd-promoted ZnZrO solid solution catalyst for CO2 hydrogenation to methanol. *Appl. Catal., B* **2022**, *304*, No. 120994.
(43) Xu, D.; Hong, X.; Liu, G. Highly dispersed metal doping to ZnZr oxide catalyst for CO2 hydrogenation to methanol: Insight into hydrogen spillover. *J. Catal.* **2021**, *393*, 207−214.
(44) Li, W.; Huang, H.; Li, H.; Zhang, W.; Liu, H. Facile synthesis of pure monoclinic and tetragonal zirconia nanoparticles and their phase effects on the behavior of supported molybdena catalysts for methanol-selective oxidation. *Langmuir* **2008**, *24*, 8358−8366.
(45) Syzgantseva, O. A.; Calatayud, M.; Minot, C. Revealing the Surface Reactivity of Zirconia by Periodic DFT Calculations. *J. Phys. Chem. C* **2012**, *116*, 6636−6644.
(46) Lamberti, C.; Zecchina, A.; Groppo, E.; Bordiga, S. Probing the surfaces of heterogeneous catalysts by in situ IR spectroscopy. *Chem. Soc. Rev.* **2010**, *39*, 4951−5001.
(47) Perdew, J. P.; Burke, K.; Wang, Y. Generalized gradient approximation for the exchange-correlation hole of a many-electron system. *Phys. Rev. B* **1996**, *54*, 16533−16539.
(48) Henkelman, G.; Jonsson, H. Improved tangent estimate in the nudged elastic band method for finding minimum energy paths and saddle points. *J. Chem. Phys.* **2000**, *113*, 9978−9985.
(49) Shi, H.; Yuan, H.; Li, Z.; Wang, W.; Li, Z.; Shao, X. Low-Temperature Heterolytic Adsorption of H2 on ZnO(10$\bar{1}$0) Surface. *J. Phys. Chem. C* **2019**, *123*, 13283−13287.

https://doi.org/10.1021/jacs.3c02248
J. Am. Chem. Soc. 2023, 145, 12663−12672